INTEGRATING OCT INTO SURGICAL SYSTEMS AND MONITORING VIBRATIONS

A Thesis

by

ESTEBAN FRANCO CARBAJAL

Submitted to the Office of Graduate and Professional Studies of

Texas A&M University

in partial fulfillment of the requirements for the degree of

MASTER OF SCIENCE

Chair of Committee,	Brian E. Applegate
Committee Member,	Javier Jo
	Mark Lenox
Head of Department,	Anthony Guiseppi-Elie

May 2016

Major Subject: Biomedical Engineering

ABSTRACT

Imaging of the hearing structures can yield information regarding their function as well as insight into the abnormalities and adverse conditions that affect them. Improvements in the acquisition techniques and the quality of imaging systems can contribute to the understanding and treatment of these conditions. Optical coherence tomography (OCT) imaging technology has evolved to the point where systems can deliver 2D cross-sectional images, 3D structural volumes, and functional information regarding the motion of the sample. The information is valuable, but while research systems continue to evolve and become more advanced there is a disconnect between the researcher and the clinician. Translation of research based imaging systems into the clinical field is an important step in future development and adaptation. This thesis is focused on the development of a packaged optical coherence tomography system and the design of a phase-stable surgical microscope OCT system that can easily be introduced into the clinical field.

DEDICATION

I am extremely thankful to my advisor, Dr. Brian E. Applegate, for his guidance, support and encouragement throughout this work. I would especially like to thank Jesung, Sangmin, Wihan, Scott, Xi, Sebina, and Cory.

I would like to Dr. Javier Jo and Dr. Mark Lenox for their time to serve on my defense committee.

I dedicate this dissertation to my parents and my brother.

.

TABLE OF CONTENTS

Page

LIST OF FIGURES

Page

LIST OF TABLES

Page

1 INTRODUCTION

Optical coherence tomography (OCT) is an imaging technique that combines high-resolution imaging with fast acquisition speeds. The result is a versatile system that is able to provide structural information from biological tissues up to a few millimeters in depth thus painting a more detailed portrait of the sample. The noninvasive, non-destructive imaging capabilities allow OCT to provide a balance between imaging depth and resolution when compared to established imaging technologies such as X-ray computer tomography (CT) or magnetic resonance imaging (MRI). First developed in the early 1990's, research into OCT technologies has grown rapidly [1]. From its early origins in ophthalmic imaging, OCT has been utilized to study a number of different biological structures in both animal models and humans [2]–[9]. Evolution of OCT imaging systems to the Fourier domain has led to systems with faster acquisition speeds and higher sensitivities [10], [11]. Functional imaging capabilities have been explored over time and can provide insight to how the imaged structures operate [8]. This adds to the overall value of the data available from OCT imaging systems.

While the technology continues to grow it has expanded to the clinical-research field. This requires the systems to progress from the laboratory benchtop and adapt to real-world situations. Clinical use of OCT for ophthalmology began in 1997; however the market is still significantly geared toward benchtop systems. Companies that are actively developing OCT systems number less than 40 [1].

For efficient adaptation into the medical field, OCT imaging technology should be made as convinient as possible. Adapting new technology to existing equipment that is already located in the meidcal setting is the best approach for deploying prototype systems for the purposes of collecting data and testing.

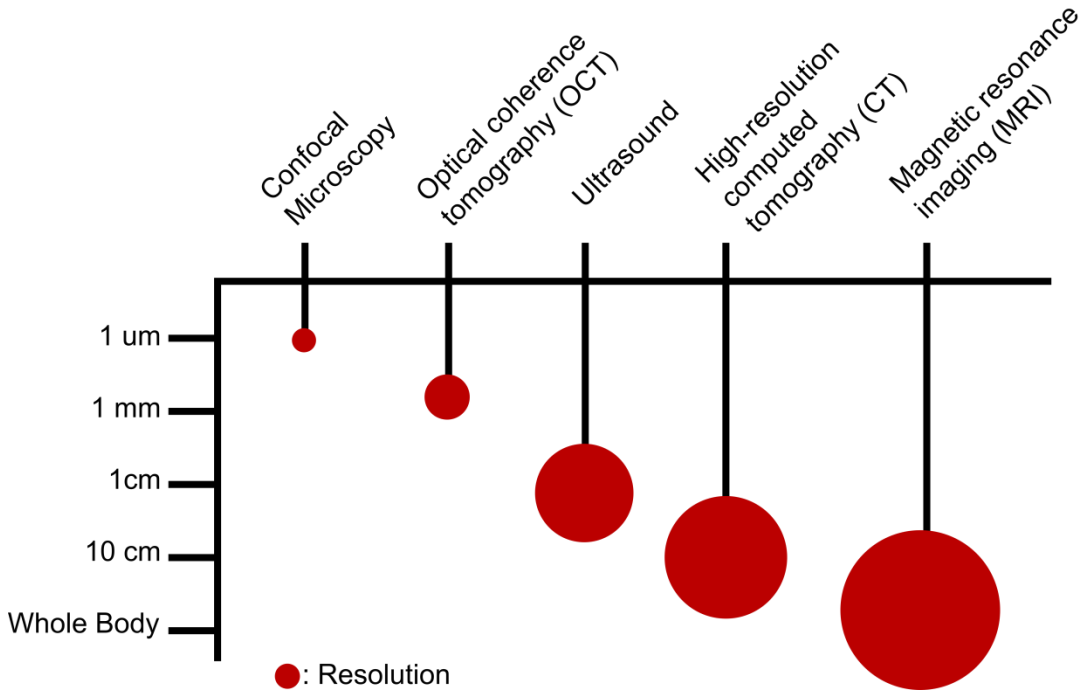

Figure 1.1: Comparison of different imaging systems in terms of resolution and imaging depth.

2 THEORY OF OCT

2.1 Interferometry

Optical coherence tomography is an interferometric imaging technique that is based upon low-coherence interferometry (LCI) to detect signal from the sample of interest. A simple optical interferometer (Figure 2.1) consists of a light source that directs an incident optical wave towards a beamsplitter. A portion of the beam is sent to the sample (sample arm) and the other portion is directed towards a reference mirror (known as the reference arm). The beam in the sample arm interacts with structure within the tissue and a portion is ultimately back-scattered towards the beamsplitter. Light in the reference arm is reflected directly along the optical path by the reference arm mirror. At the beamsplitter the backreflected light from the reference arm is recombined with the backscattered light from the sample arm and the resulting beam is then analyzed by the detector. Because the light source possesses low time coherence, interference between the reference mirror and a particular layer of the sample occurs only when the difference in the optical pathlengths of the two arms is within the coherence length of the laser. The laser's coherence length is defined as the propagation distance over which the coherence significantly degrades and is determined by [12]:

$$l_c = \frac{2\ln 2}{\pi}\frac{\lambda_0^2}{\Delta\lambda}$$

where λ_0 is the central wavelength of the laser and $\Delta\lambda$ is its bandwidth. The signal that is detected is the result of a summation of the two arms of the interferometer:

$$U(t) = U_R(t) + U_S(t+\tau)$$

Here, $\tau = \Delta L/c$ is the time difference between the two arms that is directly related to the difference in the optical pathlengths. The time-average of the current output from the detector, I_D, in its complex conjugate form is given by:

$$I_D(t) = \langle |U(t)|^2 \rangle = I_R + I_S + \langle U_R(t) \cdot U_S^*(t+\tau) \rangle + \langle U_R^*(t) \cdot U_S(t+\tau) \rangle$$
$$= \langle I_R \rangle + \langle I_S \rangle + G_{RS}(\tau)$$

Here, G_{RS}, represents the interferogram and is equivalent to twice the real argument of the cross-correlation of the analytic signal from the two interfering beams:

$$I_D(t) = I_R + I_S + 2\mathrm{Re}[\Gamma_{RS}(\tau)]$$
$$= I_R + I_S + 2\sqrt{\langle I_R(t)\langle I_S(t)\rangle\rangle}|\gamma_{RS}(t+\tau)|\cos(\alpha_{RS} - \delta_{RS}(t+\tau))$$

here the first two terms represent the intensities from the reference and sample arms, the third term describes the degree of coherence, $\gamma_{RS}(t+\tau)$ is the complex degree of coherence, the final term represents the phase where α_{RS} is the constant phase and δ_{RS} is the phase delay.

The coherence function $\Gamma_{RS}(\tau)$ can be obtained from analytic continuation:

$$\Gamma_{RS}(t) = \frac{1}{2} I_D(t) + \frac{i}{2} HT\{I_D(t)\}$$

Here, HT is the Hilbert Transform. The intensity of light measured by the detector is quantified by the current output of the photodiode. The photodiode signal is measured as current because the measurement is generally more linear than voltage measurements. Most commercial photodiode detectors utilize a transimpedance amplifier circuit to convert the current to a voltage measurement. The OCT signal then is represented by:

$$i_G(\mathrm{t}) = \frac{q_e \eta}{h\bar{\nu}} \int_{Ar(r)} G_{RS}(r,t) d^2 r$$

q_e is the quantum charge, η is the quantum efficiency, h is Planck's constant, ν is the average optical frequency and $Ar(r)$ is the area of detector sensitivity.

When the detector's surface is coplanar to the wavefronts of the interferometer beams the OCT signal (G_{RS}) is equal to the current. Therefore, the magnitude of the coherence function can be calculated as:

$$A_\Gamma(t) = \frac{1}{2} \sqrt{(G_{RS}(t))^2 + (\mathrm{HT}\{G_{RS}(t)\})^2}$$

and the phase representation is,

$$\Phi_\Gamma(t) = \tan^{-1}\left(\frac{\mathrm{HT}\{G_{RS}(t)\}}{G_{RS}(t)}\right)$$

Analysis of the correlation function will yield spectral relations via the Wiener-Khintchine theorem. A corollary of the theorem states that the power spectrum of the light wave is equivalent to the Fourier transform of its auto-correlation function,

$$S(v) = \mathrm{FT}\{\Gamma(\tau)\}$$

Additionally, the cross-spectral density of two waves can be calculated by the Fourier transform of the cross-correlation function:

$W_{RS}(v) = \mathrm{FT}\{\Gamma_{RS}(\tau)\}$,

this yields the spectral interference law:

$$S(v;\Delta t) = S_R(v) + S_S(v) + 2\mathrm{Re}[W_{RS}(v)]\cos(2\pi v \Delta t)$$

Here, Δt is the interferometric time delay.

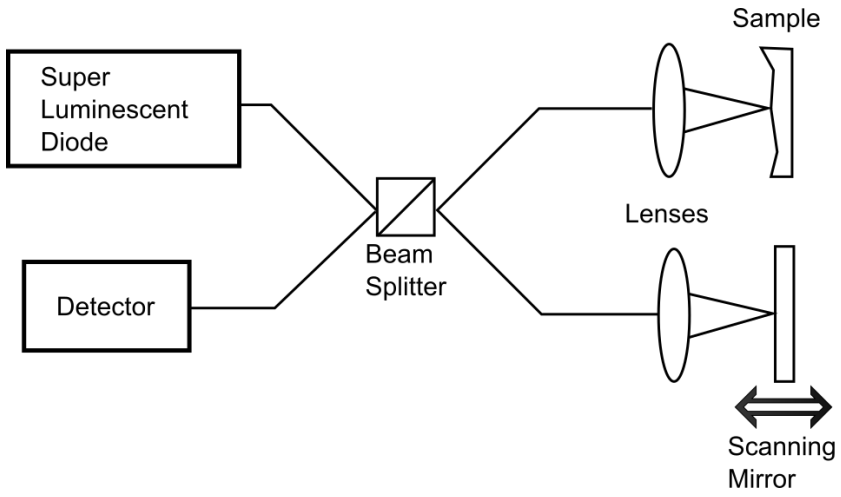

Figure 2.1: Basic schematic of LCI system. BS – Beamsplitter, λ_c – Central wavelength of laser source, $\Delta\lambda$ – Bandwidth of laser source

2.2 Time Domain Optical Coherence Tomography

The first introduction of OCT came about in 1991 with a time-domain OCT (TDOCT) system that acquired depth information from the sample by scanning the reference arm of the Michelson interferometer [13]. As stated earlier, OCT systems utilize low-coherence sources which results in interferogram formation only when the two beam paths are closely matched within the coherence length of the laser. The sample response function ($h(t)$) is convolved with the source coherence function

$$G_{RS}(t) = 2\mathrm{Re}[\Gamma_{Source}(\tau) * h(t)]$$

which allows for the intensity at some specific depth to be represented as

$$I_D(z_R) = \frac{\rho}{4}(S_0(R_R + R_{S1} + R_{S2} + \cdots + R_{Sn}) + \frac{\rho}{2}\left[S_0 \sum_{n=1}^{N} \sqrt{R_R R_S} e^{-(z_R - z_{Sn})^2 \Delta k^2} \cos(2k_0(z_R - z_{Sn}))\right]$$

This equation describes the fringe amplitude and frequency that is then used to construct a depth profile of that point in the sample (Ascan). Two-dimensional Bscans and three-dimensional Cscans are accomplished by utilizing a scanning mirror scheme such as galvanometers, a voice-coil steering mirror, or microelectromechanical system (MEMS) to perform transverse scanning in the X and Y dimensions. Translational scanning of the reference arm usually limits the maximum imaging speed of TDOCT systems however the technique is still used for several ophthalmic applications due to the ability to provide large imaging depths.

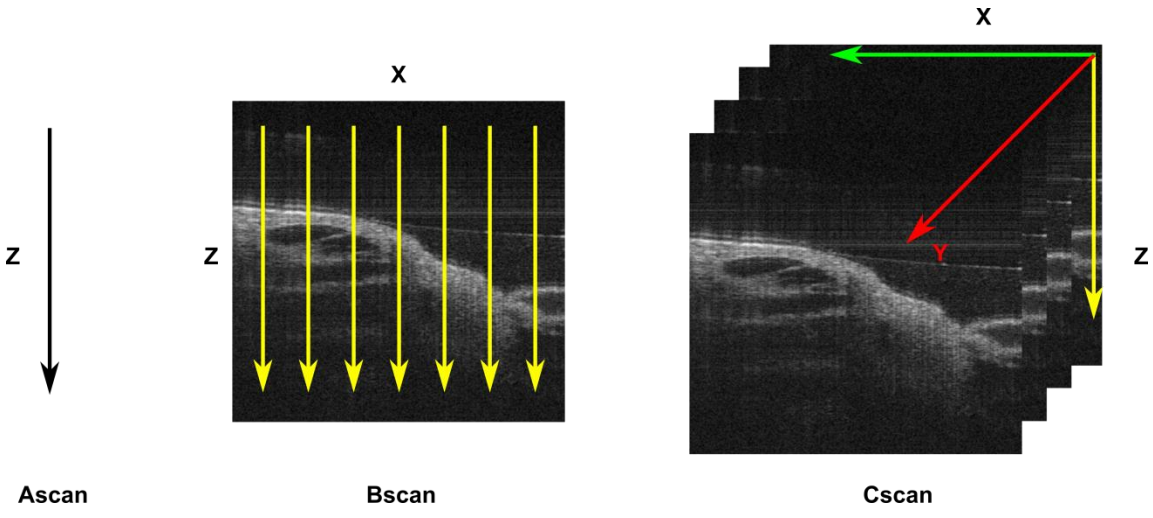

Figure 2.2: Imaging modes that are possible with OCT.

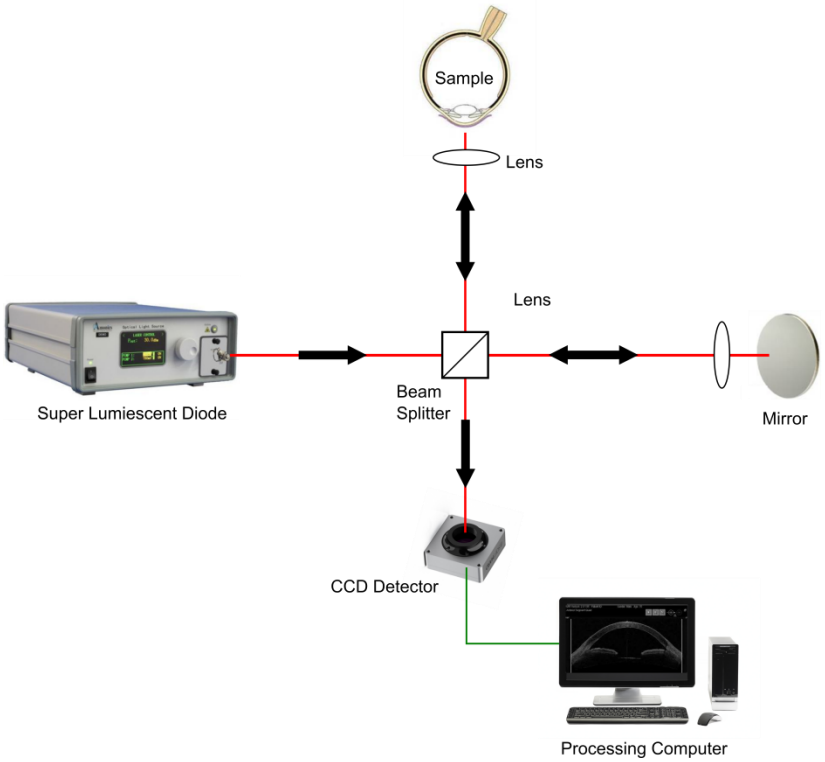

Figure 2.3: Basic schematic of time domain OCT (TDOCT) imaging system.

2.3 Frequency Domain Optical Coherence Tomography

A revolution in OCT imaging came in the form of Frequency-Domain Optical Coherence Tomography (also known as Fourier-Domain; FDOCT) [9]. While TDOCT provided high-resolution depth information, the slow imaging speed prevented it from real-time data acquisition. With FDOCT the depth information that had previously been obtained by scanning the mirror in the reference arm could now be collected all at once via an inverse Fourier transform of the spectrum of the backscattered light. The spectrum could be encoded either

spatially or in time. This allowed for the introduction of new OCT systems that possessed higher speeds and better sensitivity.

2.3.1 Spectral Domain OCT (SDOCT)

When the depth information from the interferogram is encoded spatially the OCT system is known as spectral domain OCT (SDOCT). The components of a SDOCT system include a broadband continuous laser source and spectrometer as the detector rather than a photodiode. The spectrometer is comprised of a diffraction grating, a focusing lens, and charge-coupled device (CCD) or complimentary metal-oxide-semiconductor (CMOS) detector. The separation of the source spectrum is generally performed as a linear function of wavelengths instead of k-space. Resampling of the data is required during processing prior to performing the Fourier transform.

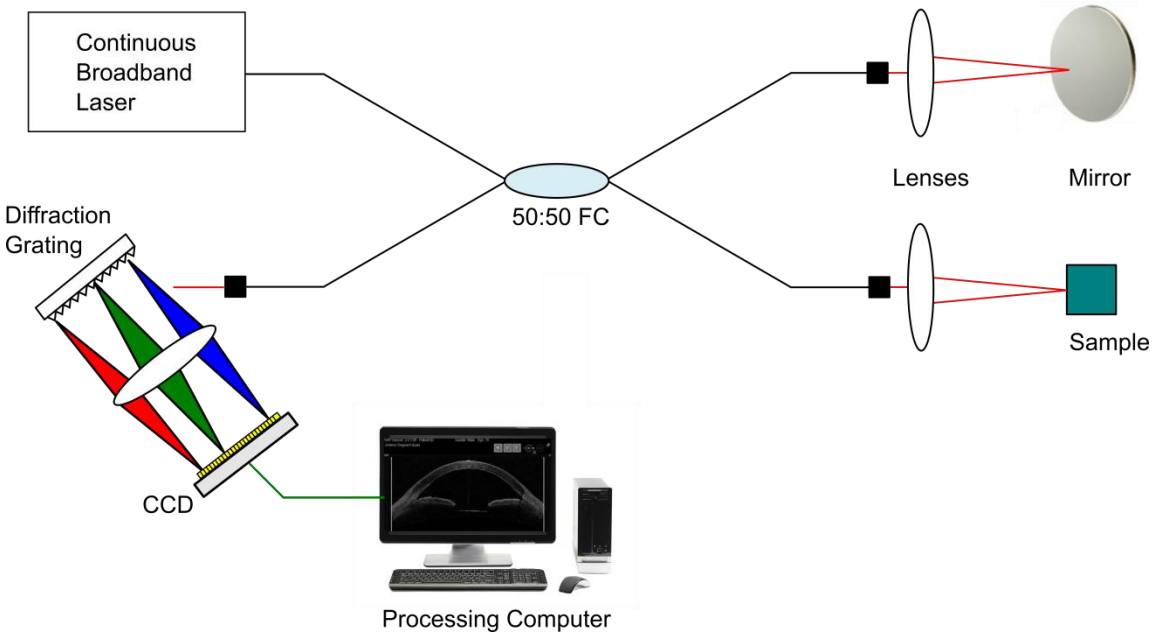

Figure 2.4: Basic schematic of a spectral domain OCT (SDOCT) imaging system. FC – Fiber Coupler. CCD – Charge-Coupled Device.

2.3.2 Swept-Source OCT (SSOCT)

The method of encoding the depth-information is in time. This type of system is known as swept-source OCT (SSOCT) or optical frequency domain imaging (OFDI). As the name implies, the source is a wavelength-swept laser that quickly cycles through a range of wavelengths and uses a narrowband filter to allow only one wavelength to be sent from the laser at a time. The full depth-information is collected at one time and removes the need to mechanically translate the reference arm mirror. A photodiode is employed rather than a spectrometer which simplifies the detection setup. Just as with the diffraction of

the source in SDOCT, the SSOCT laser's sweep is not linear in k-space and requires linearization of the acquired data prior to Fourier transformation.

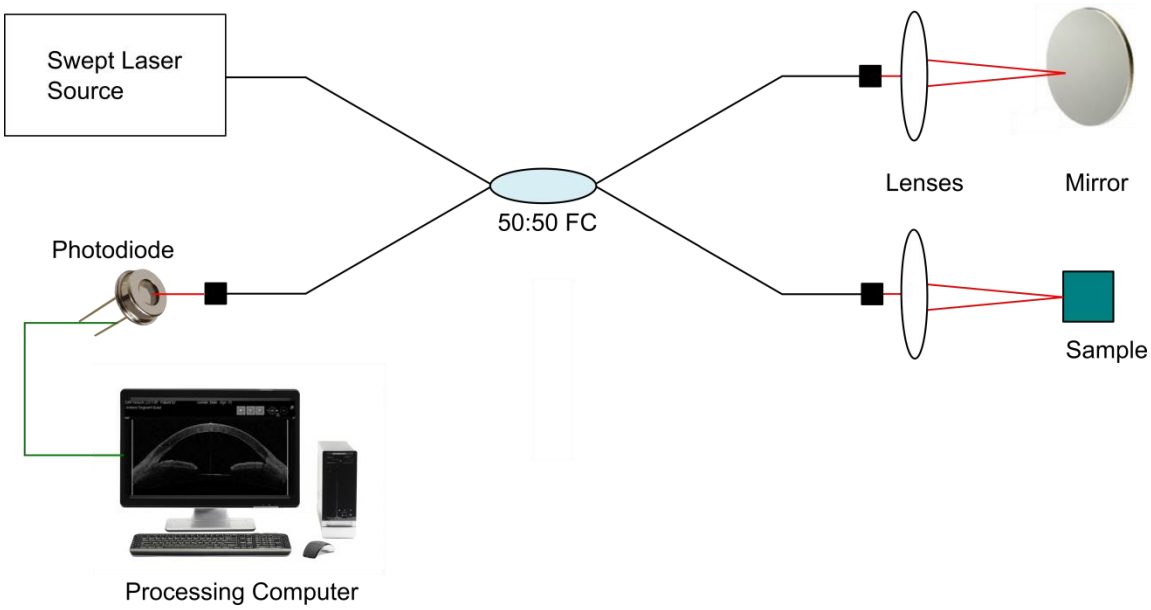

Figure 2.5: Basic schematic of swept source OCT (SSOCT) imaging system. FC – Fiber Coupler.

2.4 Specifications of OCT Systems

The specifications of OCT systems are useful for determining what system should be designed for the sample of interest. These parameters include axial and lateral resolution, imaging depth, data acquisition speed, system sensitivity, and phase sensitivity.

2.4.1 Axial Resolution

Use of low-coherence optical sources in OCT yields signal detection when the optical pathlength difference between the reference and sample arm of the interferometer is within the coherence length of the laser. Therefore the axial resolution (Δz) of an OCT system is limited by the same coherence length that is simply the Fourier transform of the source spectrum. For an approximation with a Gaussian source, the coherence length is calculated as,

$$\Delta z = \frac{2 \ln 2}{\pi} \frac{\lambda_0^2}{\Delta \lambda}$$

The central wavelength and bandwidth of the source are the only two variables that are used to calculate the axial resolution limit of the OCT system which is a departure from other optical imaging modalities, where the resolution depends on the characteristics of the optics used in the system. The axial resolution is often degraded by a mismatch in the dispersion between the reference and sample arms. Different methods of dispersion compensation are used to address this issue.

2.4.2 Lateral Resolution

The lateral resolution of an OCT system is generally calculated assuming that Gaussian profile of the input beam. More accurate calculations have been performed when the sample arm of the interferometer is likened to a reflection-

mode scanning confocal microscope. The diffraction pattern from a circular aperture can be calculated by,

$$\mathrm{I}(\theta)=\mathrm{I}_0\left(\frac{2\mathrm{J}_1(ka\sin\theta)}{ka\sin\theta}\right)^2$$

Here, k is the wavenumber and is equal to $2\pi/\lambda$, a is the aperture's radius, θ is the angle of observation, and J_1 is a first order Bessel function. This Bessel function determines the location of the lowest intensities (dark rings) of the diffraction pattern when it is equal to 0. The lateral resolution is set to be the full-width half maximum (x_{FWHM}) of the first-order Bessel function; therefore the location of the first dark ring is located at $x_{\mathrm{FWHM}} \approx 3.83$. The lateral resolution of a diffraction-limited system can also be calculated by using Abbe's law ($\Delta x = 1.22\,\lambda/2NA$) and therefore can be calculated by solving for a:

$$x_{\mathrm{FWHM}} = ka\sin\theta \approx 3.83 \;\rightarrow\; \sin\theta \;\approx\; \frac{1.22\lambda}{2a}$$

From this point, the definition of the numerical aperture is recalled ($NA = \sin\theta$) to finalize the calculation:

$$r_{lateral} = a \approx \frac{0.61\lambda}{NA}$$

The point-scanning mechanism scheme used in OCT is similar to that found in reflectance microscopy. Accordingly, areas of the sample that are within the shared volume of the illumination and detection point-spread-function are

detected. Under the assumption of a Gaussian profile from the input beam, the lateral resolution of the OCT system is defined as:

$$r_{lateral} = \frac{\sqrt{2\ln 2}}{\pi}\frac{\lambda}{NA} \approx \frac{0.37\lambda}{NA}$$

Generally, OCT systems utilize low NA objectives and try to match the lateral resolution to the axial resolution to achieve isotropic imaging of the sample [14]. However in some applications differences between the lateral and axial resolution can differ by a factor of two or more [15], [16]. An objective with a higher NA will yield in a higher resolution but at the cost of reducing the depth-of-focus of the beam.

2.4.3 Imaging Depth

The total imaging range is limited by sensitivity fall-off is described by the equation below:

$$z_{6dB} = \frac{\ln(2)}{\pi}\frac{{\lambda_0}^2}{\delta_r\lambda}$$

Here $\delta_r\lambda$ represents the full-width half maximum (FWHM) of the spectral resolution which is limited in SSOCT by the instantaneous line-width of the laser source. For SDOCT, $\delta_r\lambda$ is the spectral resolution of the spectrometer and stems from the pixel spacing of the CCD. This is convolved with the spectral interferogram to calculate the sensitivity fall-off. The theoretical imaging depth can be estimated as:

$$z_{max} = \frac{{\lambda_0}^2}{4\delta\lambda}$$

Here, $\delta\lambda$ is the spectral resolution. The spectral resolution determines the Nyquist criterion and thus limits the imaging depth.

2.4.4 Imaging Speed

The imaging speed of TDOCT systems is limited by the mechanical movement of the reference arm for the depth scan. The slow scanning speeds prevented real-time imaging. FDOCT systems revolutionized the imaging speed by eliminating the need to mechanically scan the reference arm mirror. For SDOCT systems the entire depth scan is acquired as at once by a single frame from the CCD. In SSOCT systems, the imaging speed is equal to the sweep speed of the laser source.

2.4.5 Signal-to-Noise Ratio

The signal-to-noise ratio (SNR) is very important for obtaining the best possible image from biological tissues. Generally, the interferometric signal is quantified by the mean photocurrent from the detector and the various sources of noise are the variance of the photocurrent. The current from a single detector is characterized as:

$$\langle I_s^2 \rangle = 2\rho^2 P_r P_s$$

here p represents the detector's sensitivity and the P terms represent the respective power components from the reference and sample arms of the interferometer. The system noise is characterized as a summation of a number of noise sources which generally include: receiver noise, shot noise, and excess intensity noise. Thus the system noise is described as [17]:

$$\sigma_i^2 = \sigma_{re}^2 + \sigma_{sh}^2 + \sigma_{ex}^2$$

Manufacturer specifications tend to include the receiver noise and the shot noise can be calculated as $\sigma_{sh}^2 = 2qI_{dc}B$ where q is the electric quanta, I_{dc} is the mean detector photocurrent, and B is the electronic bandwidth of the detector. The excess intensity can be determined from $\sigma_{ex}^2 = (1 + V^2)I_{dc}^2 B/\Delta\upsilon$, with V representing the degree of polarization of the source and Δv the effective linewidth of the source. Finally, the SNR of the system can be calculated as $SNR = \langle I_S^2 \rangle / \sigma_i^2$.

Common-mode noise can be removed by using a balanced detection scheme in which two detectors are employed. The remaining component of the excess sensitivity noise is described as $\sigma_{be}^2 = 2\,(1 + V^2)\rho P_r \rho P_x B/\Delta\upsilon$, and is referred to as the beat noise. The resulting total photocurrent variance is therefore $\sigma_i^2 = 2(\sigma_{re}^2 + \sigma_{sh}^2 + \sigma_{be}^2)$. The extra factor of two stems from the use of two independent detectors whose variances sum together. The measured intensity in the balanced configuration can be determined from $\langle I_s^2 \rangle = 8\rho^2 P_r P_s$. This

increased signal from the balanced detection scheme yields higher system sensitivity.

Fourier Domain OCT introduced a huge improvement for OCT imaging systems. Enhancements in imaging speed and system sensitivity allowed FDOCT systems to become the leading system technology. The performance advantage of FDOCT systems over TDOCT was described Leitgeb *et al.* In SDOCT systems the peak signal intensity is described as [10]:

$$S(\tau)_{FDOCT}^{Peak} = \frac{\rho n \tau}{h\nu_0}\frac{P_0}{N}\sqrt{\gamma_r \gamma_s R_r R_s}$$

Here, ρ is the detector responsivity, τ is the detector integration time, and N is the number of pixels on the CCD that are used by the spectrometer. At first it may seem that the peak signal intensity is lower for the SDOCT system but the noise is also decreased by 1/N as a result of a normalization factor from the DFT.

$$\sigma_{i-SDOCT}^2 = 1/N(\sigma_{re}^2 + \sigma_{sh}^2 + \sigma_{ex}^2)$$

As a result, the SDOCT system will have a sensitivity advantage over TDOCT systems.

SSOCT also possess a sensitivity advantage over TDOCT which has been described by Choma *et al* [11]. The SNR of the SSOCT system is tied to the number of samples collected:

$$SNR_{SSOCT} = M\frac{\rho R_S S_{TDOCT}}{4eB_{SSOCT}}$$

The equation shows a $M/4$ improvement of the signal for the SSOCT system. In addition, the signal and noise equivalent bandwidth of the SSOCT system (S_{SSOCT} and B_{SSOCT}, respectively) both scale linearly with M and allows the sensitivity to be independent of both the scan depth and the bandwidth of the source. TDOCT systems have an inverse proportionality with both of these parameters.

2.4.6 Phase Measurements

In addition to depth information regarding the structure of the sample, it is possible to acquire functional information as well. The acquisition of phase information from the data is useful in visualizing motion of the sample. This technique has been used to monitor the axial velocity of red blood cells in vessels [18]–[22] and also vibrations that occur in the small structures of the inner-ear [8], [23]. Phase measurements are made by comparing the difference between successive scans therefore it is important to reduce interferometric and systematic instabilities. SDOCT systems have inherent phase stability due to the lack of moving parts in its components such as the light source and the spectrometer. SSOCT systems however are more susceptible to phase noise introduced by inter-sweep variability of the laser source. A number of methodologies have been employed to improve the phase stability of the system including use of a stable mirror in the “calibration” arm to use as a phase

reference [24]. This method works by monitoring both the sample and calibration arms and removing the common phase noise that is seen. The assumption that the mirror in the calibration arm remains completely still allows for the generation of a phase correction. Another method works by shifting the collected data to a known reference point in order to correct any timing errors that might have occurred. A point in the dataset that occurs at a known point in time can be used to shift all data by a certain number of points to align each dataset. This removes all time variation and phase-stabilizes the dataset [25].

The overall sensitivity of the OCT system can be calculated from the SNR and the central wavelength of the source [26] and is based upon the intensity of the Ascan and the Fourier transform of the white-noise term. The relationship between the noise and signal is seen exactly the same as SNR which yields the sensitivity which can be described as:

$$\delta x_{sens} = \frac{\lambda}{4\pi n\sqrt{2}}\sqrt{\frac{1}{SNR}}$$

Here, n is the refractive index of the sample.

Mscans are used to collect phase measurements. An Mscan is similar to an Ascan except that rather than acquiring only one instance of data, a large number of samples are acquired over a specified time period from one position. By imaging this way the change in the structure can be monitored over time.

2.5 Monitoring Vibrations with OCT

Hearing loss affects one of the five main senses and is important in everyday interactions and in having a high quality of life. Speech recognition, music appreciation, and learning are all negatively affected. Combat zones expose soldiers to a wide variety of loud noise sources including engine noise, weapon fire, and explosions. Of particular importance are improvised explosive devices (IEDs) which are not only terribly dangerous with their primary blast, but their secondary shockwave can cause negative side effects in the form of damage to the hair cells. The mechanisms of the internal structures of the inner-ear such as the organ of Corti (OC) are still not fully understood due to the lack of ability to monitor the structure and motion of the OC. Previous studies have demonstrated the use of laser Doppler Vibrometry (LDV) to monitor the motion of the small structures within the OC at a nanometer scale [27]–[30]. The drawback of LDV is that the output is a graph that must be interpreted because they do not provide a clear image of exactly what structure is currently being imaged nor what in-depth surfaces are being monitored.

Despite these limitations, the ear functionality has remained an area of interest. OCT has been employed for imaging these structures and monitoring the phase changes that are induced by tissue motion [31]–[33]. Because of this major advantage over other imaging systems, OCT remains a popular option for the study of the OC structure and function.

3 IMPLEMENTATION

3.1 Portable Fiber Optic OCT System #1

The OCT system was first constructed on an optical table and was later compacted to fit inside a rolling cart for mobility. The fiber-based system utilizes a wavelength-swept laser source (SSOCT-1300; Axsun Technologies, Inc.) that progresses through the 100 nm wavelength range at a speed of 50 kHz with a spectrum centered at 1310 nm and an output power of 20 mW. The output is directed into a fiber coupler that splits the source intensity into two unbalanced paths. The first path receives ten percent of the total source intensity and is sent to a fiber-Bragg grating (FBG). The FBG functions by reflecting a very narrow specific wavelength range (<1 nm) from the input while allowing the rest of the wavelength range to pass undisturbed to the Mach-Zehnder interferometer (MZI) optical clock. The MZI optical clock (INT-MZI-1300; Thorlabs, Inc.) is an off-the-shelf subassembly that generates a calibration signal that is used for data processing. The other arm of the fiber coupler is passed to another fiber coupler that splits the remaining light into a 99:1 ratio to form the sample and reference arms of the primary Mach-Zehnder interferometer. The main portion of the light passes through the first port of an optical fiber circulator (CIR-1310-50-APC; Thorlabs, Inc.) that functions by directing light through different fiber ports sequentially. The light is then directed to the imaging setup of the system which focuses and scans the imaging beam on the sample for data acquisition. The one percent portion of the fiber coupler is used for the reference arm of the

interferometer. This light passes through a polarization controller to match the polarization state of the returning light from the sample arm in order to maximize the detected signal's intensity. The light is further conditioned with a fiber-based attenuator to reduce the intensity of the light from the reference arm and avoid signal saturation. Finally, an optical delay line is used as the reference arm mirror and can be finely adjusted for zeroing the optical pathlength difference between the two arms of the interferometer. The light from the paths are then combined via a 50:50 fiber coupler where they interact to form an interferogram which is then detected by the photodiode detector (PDB460C; Thorlabs, Inc). The signal from the detector is digitized by a 14-bit digitizer (NI-5761; National Instruments) with a sampling rate of 250 MS/s and is connected to an FPGA module (NI PXIe-7965R FlexRIO; National Instruments, Inc.). Two channels of the digitizer were used, one for the MZI optical clock signal and the other for the interference signal from the photodetector.

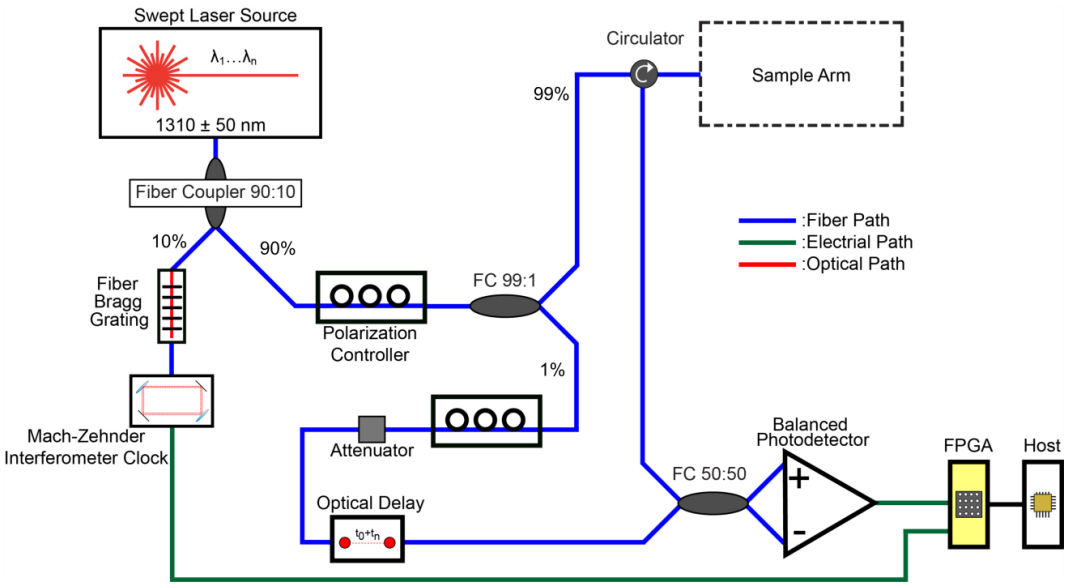

Figure 3.1: Schematic of swept source OCT (SSOCT) system. FC – Fiber Coupler. FPGA – Field Programmable Gate Array.

The fiber-based system design makes it relatively simple to change the imaging scheme of the sample arm. This is useful when different imaging schemas are used for a clinical research setting and the operating room.

3.1.1 Research Microscope Mounted Imaging System

For the clinical setting the imaging system is combined with a Zeiss SteREO V8 dissecting microscope that is similar to microscopes commonly found in research laboratories. The one-piece sample arm is attached to the microscope with optical paths of the microscope and imaging system common upon the sample. This allows the user to view the sample and the location of the imaging beam simultaneously. The transverse scanning mechanism is mounted onto the

microscope. A voice-coil steering mirror allows for scanning of the beam on the sample. Two focusing objectives are available for imaging and provide the option of achieving better lateral resolution imaging at the expense of working distance. The stock Zeiss objective provided a focal length of 63 mm while a custom designed objective was used for better resolution. The custom objective featured a triple lens configuration (Figure 3.2) that delivers 12 μm lateral resolution while minimizing chromatic and spherical aberrations throughout the scan range (Figure 3.3 A-D).

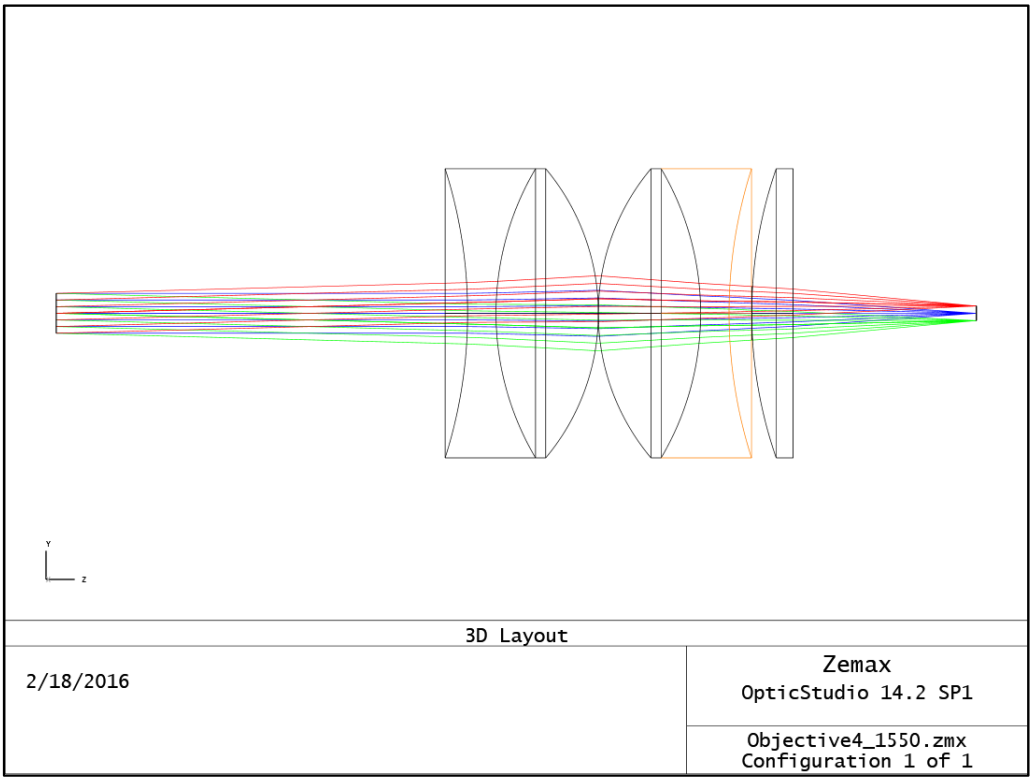

Figure 3.2: Zemax model of clinical optical system. Lenses are two AC508-150-C and one LA1417.

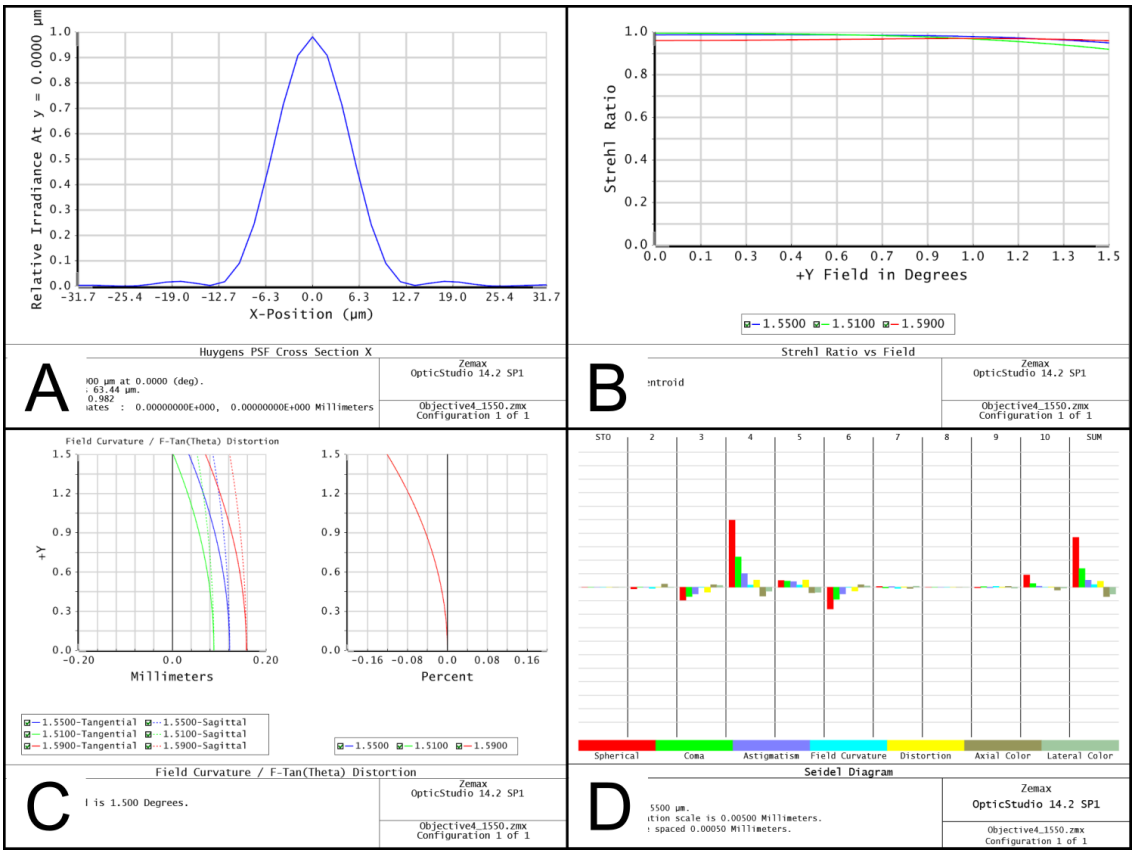

Figure 3.3: Zemax report of clinical optical system. (A) Huyen's PSF Cross Section depicting FWHM and Strehl ratio. (B) Strehl Ratio vs. Scan Angle shows the beam quality throughout the scan range. (C) Field Curvature for each wavelength and the chromatic aberration – max curvature of 400 µm. (D) Seidel Diagram graphically depicts different types of aberrations introduced by each surface of the optical system with a cumulative total at the end – y-axis scale is 5 µm and max spherical aberration is 16 µm.

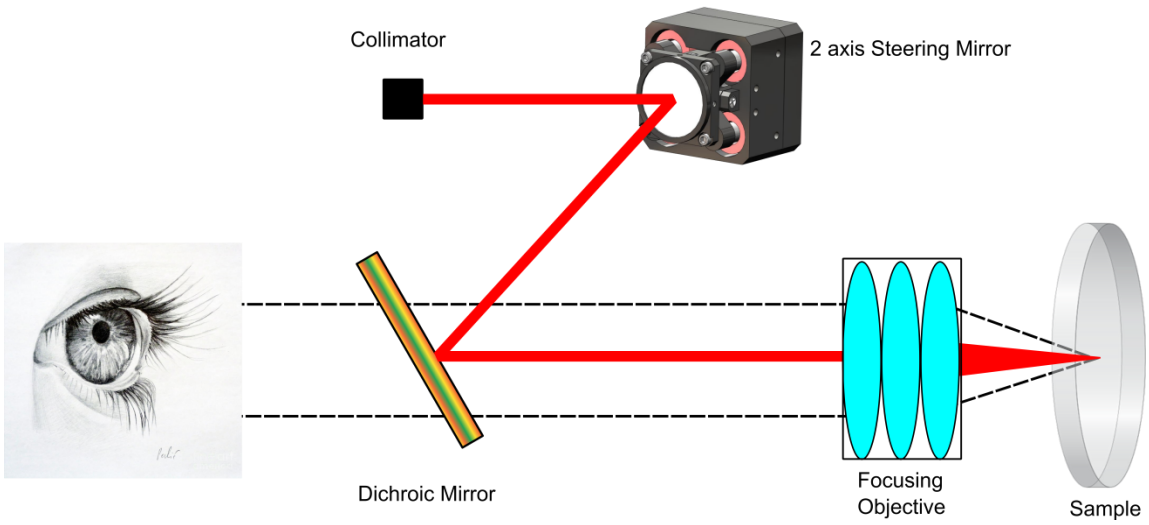

Figure 3.4: Research Microscope Mounted OCT imaging system. Scanning is performed with two-axis voice coil steering mirror which provides excellent beam stability. Dichroic mirror reflects near-infrared light while transmitting light from the visible range; this allows the sample to be imaged and viewed simultaneously.

All imaging optics are encased into a 3D printed enclosure that can be easily attached to the microscope. The enclosed design ensures that no optical alignment is required after the initial assembly of the optical components and the enclosure. With computer-aided design (CAD) software, the internal features of are designed so that the all of the optical components are inherently aligned when they are installed which simplifies the overall assembly process.

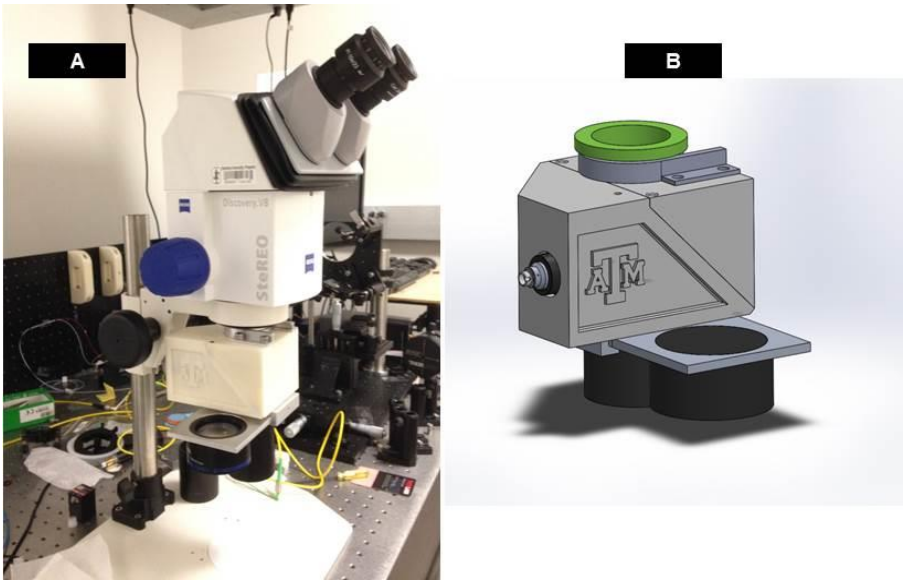

Figure 3.5: Research Microscope Mounted OCT imaging system. 3D printing allows for the housing to be designed around the required components for the optical system.

3.1.2 Operating Room Microscope Mounted Imaging System

Imaging performed during an operating room procedure requires that considerations be taken for the sterile setting and maintaining a safe environment for the patient and all personnel. Microscopes designed for the operating room are very different from those found in research laboratories. As such, the imaging optics of the OCT system must adapt to the microscope and provide similar characteristics to facilitate a simple transition from viewing through the microscope to acquiring OCT data. A Leica M400 E was the foundational model for design. Nominally the microscope features a long range focusing objective on the order of 300 mm working distance with an adjustable focal plane. The microscope itself is incorporated into a fully enclosed stand that

supports the microscope. The stand provides auto-balancing for easy positioning and the arm allows the base to be placed away from the operator to maximize working space for the operation. All of these features were taken into account during the design of the optical setup for the surgical system.

Figure 3.6: Leica M400E Surgical Microscope. The arm balances the microscope over the patient and is manually positioned by the operator. Fine-focusing is then used to precisely place the focal plane.

The optical setup of the system was comprised of a MEMS two-axis beam steering mirror (Mirrorcle, Inc.), a custom beam expander, and a custom focusing objective. The MEMS platform allows for a small form factor in the optical setup but limits the input beam to less than 3 mm. A ten lens optical system was designed in Zemax to take a FC-APC fiber input and yield an extremely long focusing length of over 300 mm while maintaining a lateral resolution of 18 μm (FWHM) and a Strehl ratio of 0.8 across the wavelength band. In addition, spherical and chromatic aberrations were minimized by combining different lens shapes such as aspheric, achromatic doublets, and

meniscus lenses. Figure 3.7 depicts the Zemax model of the optical system starting from the MEMS scanning mirror, Table 3.1 lists the lenses used in order, and Figure 3.8 shows the Zemax report of the optical system.

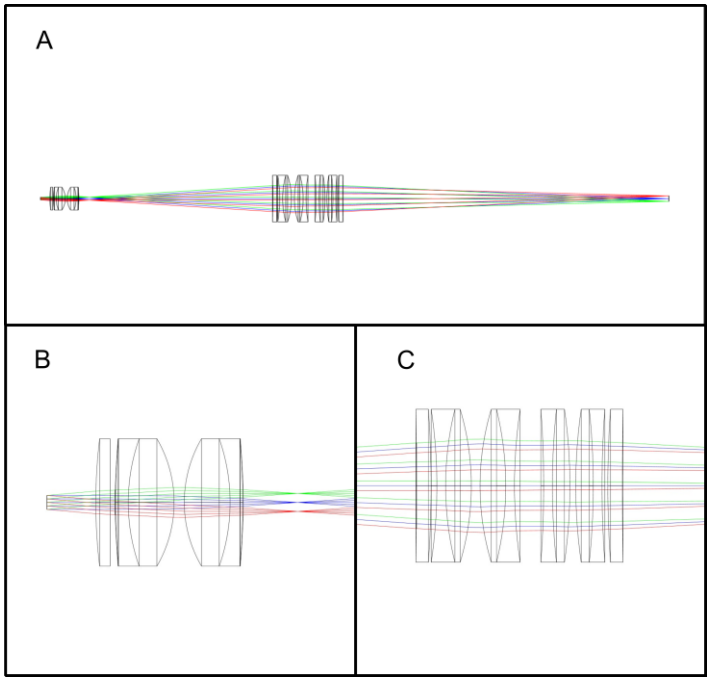

Figure 3.7: Zemax model of surgical optical system. Colors represent extremes in the scanning positions. (A) Overall system. (B) Expanding lenses. (C) Collimating lenses and focusing objective.

Table 3.1: List of lenses utilized for surgical optical system.

	EFL (mm)	**Lens Diameter (mm)**	**Manufacturer**
FC260-C	15.52	6.5	Geltech
LA1253	200	25.0	Thorlabs
49664	40	25.0	Edmund Optics
49664	40	25.0	Edmund Optics
LE4822	1000	50.8	Thorlabs
AC508-500-C	500	50.8	Thorlabs
AC508-500-C	500	50.8	Thorlabs
AC508-1000-C	1000	50.8	Thorlabs
AC508-1000-C	1000	50.8	Thorlabs
LE4822	1000	50.8	Thorlabs

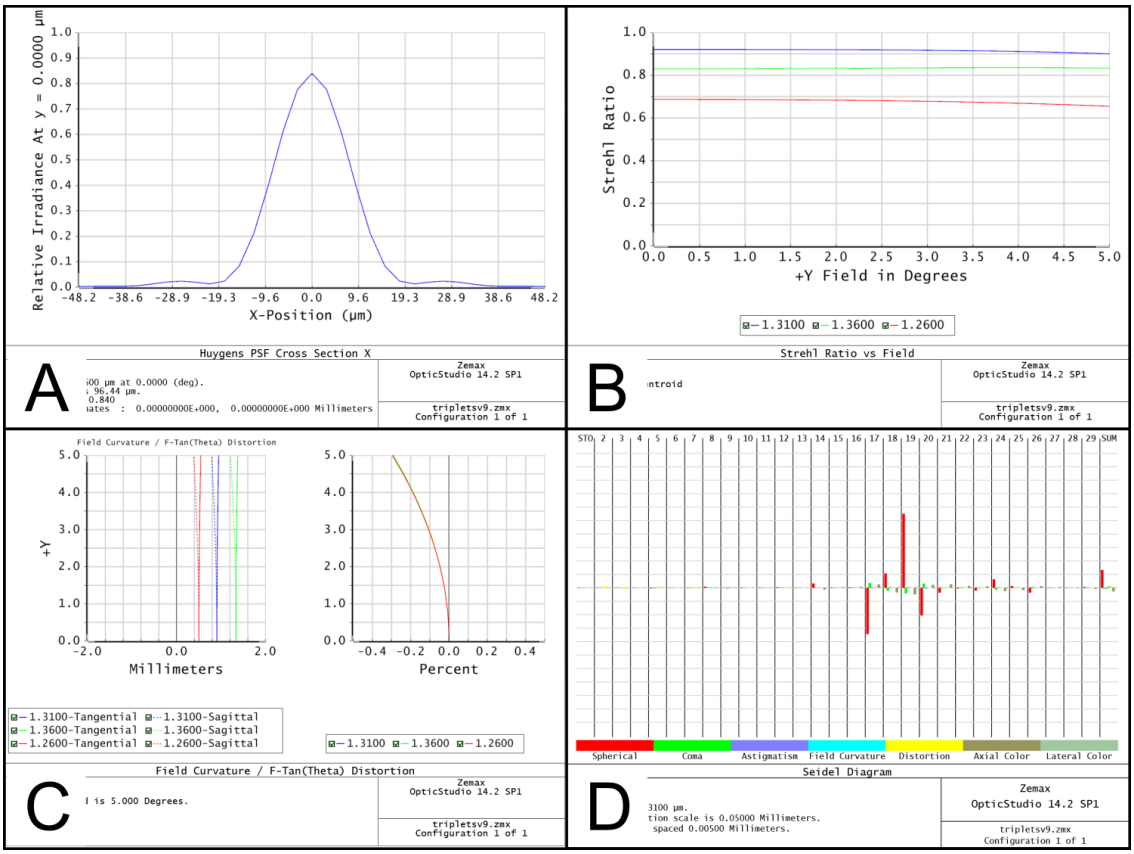

Figure 3.8: Zemax report of surgical optical system. (A) Huyen's PSF Cross Section depicting FWHM and Strehl ratio. (B) Strehl Ratio vs. Scan Angle shows the beam quality throughout the scan range. (C) Field Curvature for each wavelength and the chromatic aberration – max curvature of 300 µm. (D) Seidel Diagram graphically depicts different types of aberrations introduced by each surface of the optical system with a cumulative total at the end – y-axis scale is 50 µm and max spherical aberration is 52 µm.

In order to emulate the fine-focusing feature of surgical microscopes, the focusing group of lenses were mounted upon a translational stage that allows for the focus point to be moved a total of 25 mm. With this feature, the microscope can be roughly positioned by the operator to the region of interest by hand and then finely focused using the translational stage.

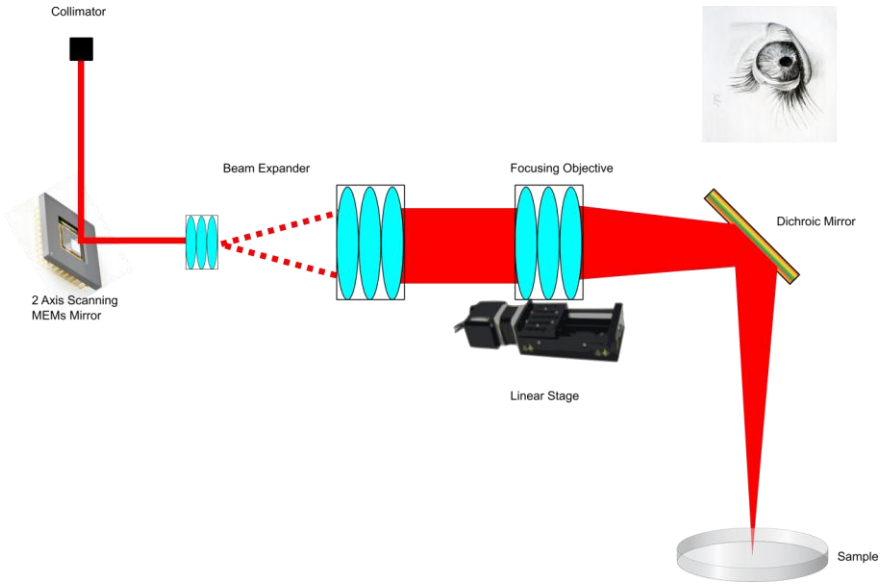

Figure 3.9: Surgical Microscope Mounted OCT imaging system. 2 axis MEMS scanning mirror used for 2D imaging. Linear stage allows for fine-positioning of the focal plane.

3.2 Fiber Optic System #2

As discussed earlier it is necessary to linearize the OCT data in k-space to preserve imaging depth and image quality. Hardware solutions are possible to overcome this challenge such as linear-in-wavenumber spectrometers for SDOCT [34], [35] and k-triggering in SSOCT [36]. The modifications in the hardware complicate construction of the OCT system. Because of this, the most common solution is to interpolate the acquired dataset to generate data that is linear in k-space before performing the fast Fourier transform (FFT). This processing step requires significant computational resources and slows down the overall real-time imaging speed.

To bypass this issue, this system utilizes a Vernier-tuned Distributed Bragg Reflector (VT-DBR) laser that is capable of providing wavelength-sweeps that are linear in k-space [37], [38]. Traditionally, swept-source lasers involve a moving structure that provides wavelength-dependent feedback that changes the emission of the laser. It is this structures that determines the maximum achievable momentum that is the fundamental limit to the sweep-speed of the laser. The VT-DBR uses changes in the refractive index of a semiconductor material to change the output wavelength and removes the momentum-based limitations on the sweep-speed. This reduces the laser's inter-sweep variability which provides a much more accurate sampling trigger. The combination of this trigger stability and the wavelength sweeps that are linear in k-space allow for a very good foundation to phase-sensitive OCT (PhOCT) imaging.

Figure 3.6 shows a schematic of the experimental system. The prototype VT-DBR laser (Akinetic Swept Laser; Insight Photonics Solution, Inc.) with a sweep speed of 45 kHz and a 90 nm bandwidth centered at 1570 nm. The output of the laser is split via a 99:1 fiber coupler with a majority of the light going to the sample arm and the remainder going through a fiber attenuator and optical delay line. The two arms of the interferometer are combined with a 50:50 coupler to form the OCT spectral interferograms which are detected with a balanced photo detector (PDB460C; Thorlabs, Inc.). The signal from the detector is acquired with a 12-bit digitizer that has a maximum sampling rate of 1.6 GS/s (NI 5772; National Instruments, Inc.) connected to an FPGA module (NI PXIe-7966R

FlexRIO; National Instruments, Inc.). Since the laser sweep is linear in k-space, only one channel of the digitizer is required. A speaker is used to deliver a test tone to the sample while simultaneously acquiring data.

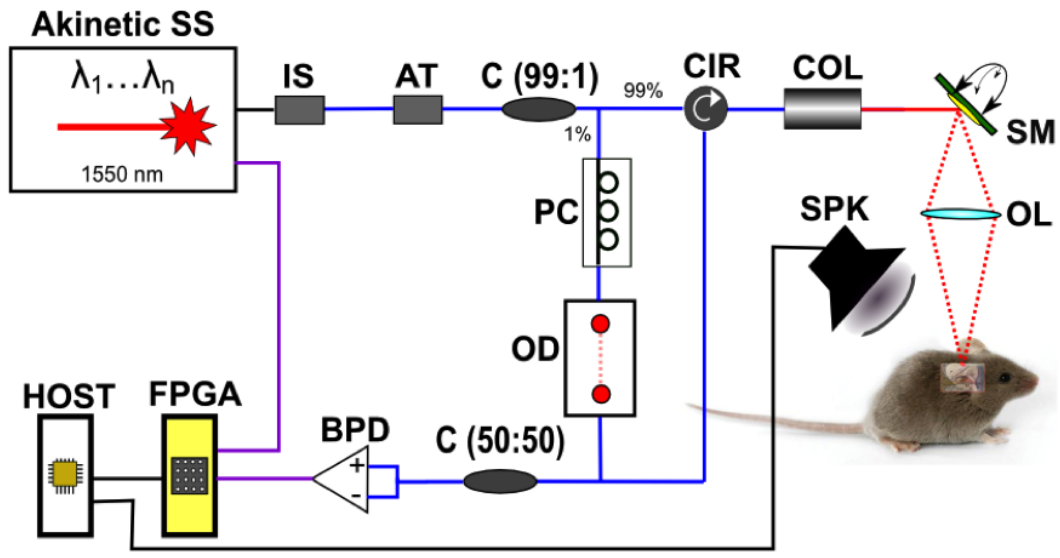

Figure 3.10: Schematic of Phase-Sensitive OCT imaging system. IS – Isolator. AT – Attenuator. CIR – Circulator. C – Fiber Coupler. COL – Collimator. SM – Scanning Mirror. OL – Objective Lens. PC – Polarization Controller. OD – Optical Delay Line. BPD – Balanced Photodetector. FPGA – Field Programmable Gate Array. SS – Swept Source Laser. SPK – Speaker. Reprinted from [39].

4 MONITORING MIDDLE-EAR MOTION WITH PHASE-SENSITIVE OCT*

The experimental system described in Section 3.2 is used for imaging the inner-ear in this chapter. For experiments, a C57BL/6 mouse was sacrificed under the protocol approved by the Texas A&M University Institute Animal Care and Use Committee. The outer ear and pinna is surgically removed under a dissecting microscope to expose the tympanic membrane for imaging. 2D and 3D images are acquired to select a region of interest. For vibration experiments, an Mscan is performed at the position-of-interest while simultaneously providing a sinusoidal sound stimulation. The Mscans were comprised of 10,000 Ascans with sound stimulus ranging from 4 – 10 kHz and 50 – 70 dB SPL. Normal OCT processing steps are performed except for data linearization which is not required due to the linear-in-k sweeps provided by the laser. The processing generates a complex Aline as a function of time. A second FFT is performed along the time axis and provided information regarding the vibration's magnitude and phase. The magnitude values, acquired in radians (rad) values were converted to units of nanometers (nm) by:

$$(\mathrm{nm}) = \lambda o/(4n\pi)$$

Here, λ_o is the central wavelength of the laser source and n is the refractive index

*Part of the data reported in this section is reprinted with permission from "Phase-sensitive optical coherence tomography using an Vernier-tuned distributed Bragg reflector swept laser in the mouse middle ear", Jesung Park, Esteban F. Carbajal, Xi Chen, and Brian E. Applegate, 2014, Optics Letters, Vol. 39, pp. 6233-6236, Copyright 2014 by OSA Publishing

of the sample which was assumed to be 1.44 [40].

Figure 4.1 shows representative volumetric and cross-sectional images of the mouse inner-ear that were acquired with the PhOCT system. The tympanic membrane and the manubrium of the malleus are easily discernible with the in-depth images. The volumetric Cscans have the dimensions of 2.4 mm × 2.4 mm × 2.6 mm (respectively, X, Y, and Z). The dotted line represents the selected region-of-interest that was selected for vibration measurements.

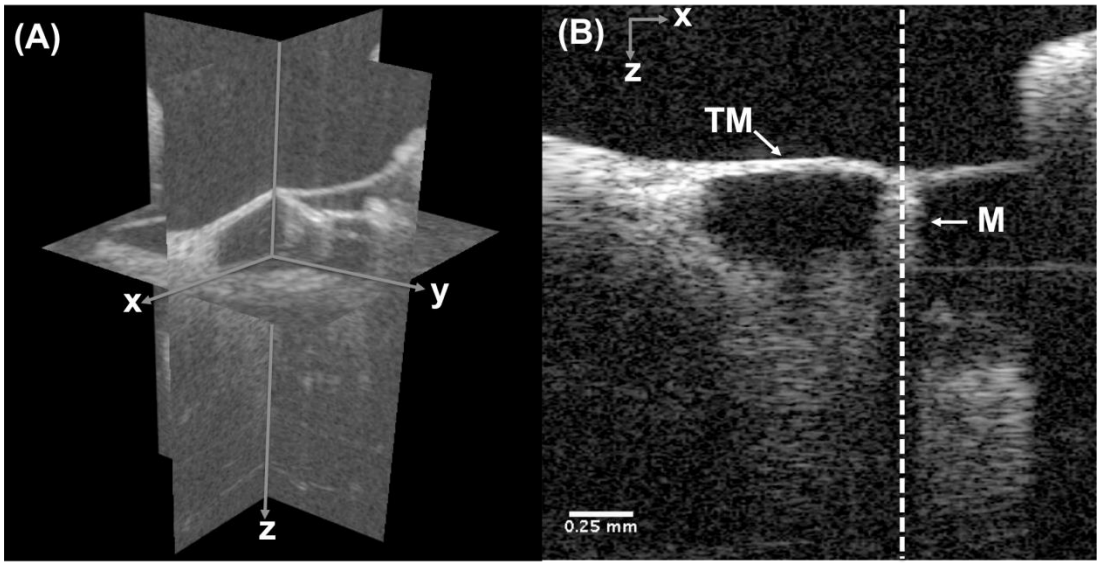

Figure 4.1: Representative volumetric (A) and cross-sectional (B) images of ex vivo mouse tympanic membrane. TM – Tympanic Membrane. M – Manubrium. White dotted line represents the position-of-interest selected for vibration measurements. Reprinted from [39].

The vibrational data measured is summarized in Figure 4.2. The frequency peaks that correspond to the stimulus frequency are clearly shown on from the

tympanic membrane due to the low overall background noise which is indicative of the system's phase stability. Vibration amplitudes for 4 kHz ranged from 1 nm at 50 dB SPL to 7 nm at 70 dB SPL and 6 nm (50 dB SPL) to 55 nm (70 dB SPL) for 8 kHz stimulus frequency.

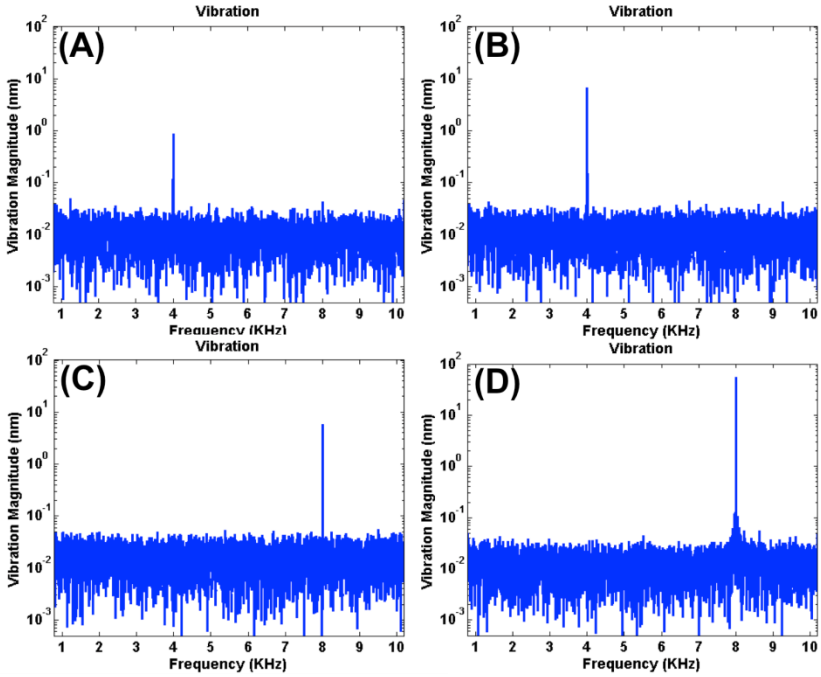

Figure 4.2: Vibration measurements of the manubrium in ex vivo mouse middle-ear. 10,000 Ascans were acquired for each combination of stimulus frequency and intensity. (A) 4 kHz at 50 dB SPL. (B) 4 kHz at 70 dB SPL. (C) 8 kHz at 50 dB SPL. (D) 8 kHz at 70 dB SPL. Measured amplitudes were: (A) ~1 nm, (B) ~7 nm, (C) ~ 6nm, and (D) ~55 nm. Reprinted from [39].

A total of 12 different stimulus signals were used with the mouse sample: 50, 60, and 70 dB SPL intensity levels at 4, 6, 8, and 10 kHz frequencies. A linear relationship between stimulus intensity and the measured vibration magnitude

was observed which is expected due to the passive nature of the tympanic membrane (Figure 4.3(A)). When the vibrational magnitude was compared to the stimulus frequency as shown in Figure 4.3(B) a bandpass filter response was noted. The filter possess a peak at 8 kHz which correlates well with other studies that utilize LDV for measuring sound induced vibrations in the a C57BL/6 mouse [41].

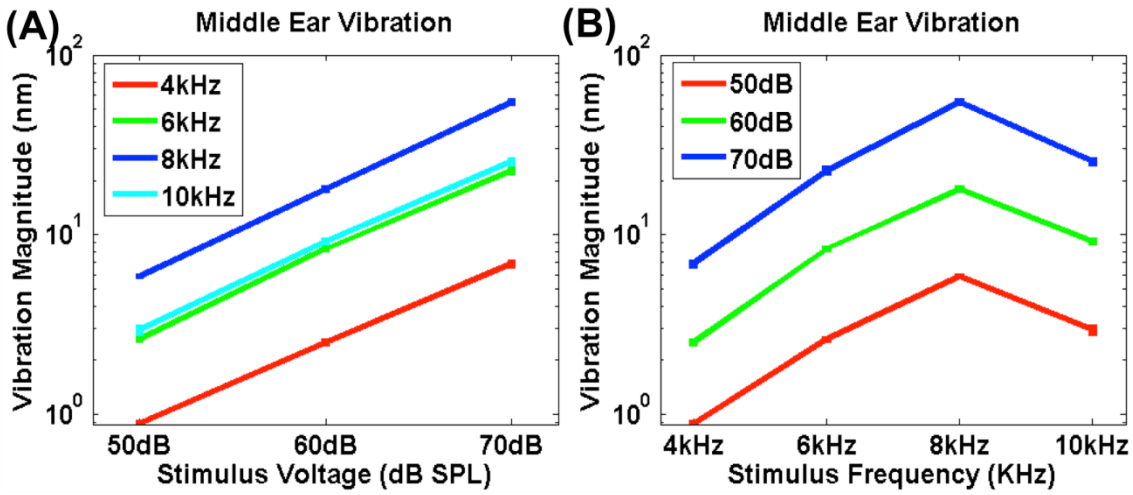

Figure 4.3: Measured vibrational magnitudes as a function of (A) stimulus intensity and (B) stimulus frequency. A linear relationship is seen in (A) which corresponds with the passive nature of the tympanic membrane. A bandpass filter response is noted in (B) with a peak at 8 kHz and correlates well with [41]. *Reprinted from* [39].

The results from these experiments demonstrate the effectiveness of utilizing a VT-DBR laser source for PhOCT. The reduction in the inter-sweep variability allows for the system to provide low phase noise and improved phase sensitivity. Additionally, the laser sweeps that were linear in k-space revised the data

processing steps by removing the need for data interpolation which allows for an increase in the overall processing speed.

5 CONCLUSIONS

Two approaches were investigated with the goal of improving clinical viability of OCT imaging systems. The first involved the use of 3D printing adapters to existing medical equipment for rapid deployment. The use of 3D printing allows for housings to be designed around the optical components and an inherent alignment. Drop-in alignment of the optical system simplifies construction and needs no further modification which eases the adaptation for medical professionals. A fast paced iterative process will be beneficial during the development phase of new medical applications. The custom optics of the systems emulated the features of the equipment that they were adapted to including long working distances and adjustable focal planes. The second approach investigated the use of an akinetic swept source laser which delivers wavelength sweeps that are linear in k-space and has a low inter-sweep variability. Using an akinetic source eliminates the need for acquiring an optical clock signal and reduces the amount of data that is needs to be collected. In addition, the interpolation step in the data processing is also not necessary and frees up the computational time and resources normally reserved for this processing step. Cross-sectional images, 3D volumes, and vibrational measurements of *ex vivo* middle ear structures demonstrated the application of a 3D printed optical housing with an akinetic swept source laser for structural and functional OCT imaging.

The results of these studies indicate that further developments into OCT technology could improve the translational efficiency of tabletop research systems to clinically applicable imaging systems. Further study is necessary for integrating of both approaches to produce a portable OCT imaging system with high phase stability even after placement and replacement during operational procedures. Robust OCT imaging systems will improve further studies into imaging and vibrational studies and increase adaptation into the medical field.

WORKS CITED

[1] "Some Historical Statistics of Academic Publications in the Field of Optical Coherence Tomography -Optical Coherence Tomography News." [Online]. Available: http://www.octnews.org/articles/4061333/some-historical-statistics-of-academic-publication/. [Accessed: 07-Sep-2015].

[2] Y. Yang, A. Dubois, X. Qin, J. Li, A. El Haj, and R. K. Wang, "Investigation of optical coherence tomography as an imaging modality in tissue engineering," *Phys. Med. Biol.*, vol. 51, no. 7, pp. 1649–1659, Apr. 2006.

[3] X. D. Li, S. A. Boppart, J. Van Dam, H. Mashimo, M. Mutinga, W. Drexler, M. Klein, C. Pitris, M. L. Krinsky, M. E. Brezinski, and J. G. Fujimoto, "Optical coherence tomography: advanced technology for the endoscopic imaging of Barrett's esophagus.," *Endoscopy*, vol. 32, no. 12, pp. 921–30, Dec. 2000.

[4] B. Colston, U. Sathyam, L. DaSilva, M. Everett, P. Stroeve, and L. Otis, "Dental OCT," *Opt. Express*, vol. 3, no. 6, p. 230, Sep. 1998.

[5] T. GAMBICHLER, G. MOUSSA, M. SAND, D. SAND, P. ALTMEYER, and K. HOFFMANN, "Applications of optical coherence tomography in dermatology," *J. Dermatol. Sci.*, vol. 40, no. 2, pp. 85–94, Nov. 2005.

[6] R. K. Manapuram, V. G. R. Manne, and K. V. Larin, "Phase-sensitive swept source optical coherence tomography for imaging and quantifying of

microbubbles in clear and scattering media," *J. Appl. Phys.*, vol. 105, no. 10, p. 102040, May 2009.

[7] E. F. Carbajal, S. A. Baranov, V. G. R. Manne, E. D. Young, A. J. Lazar, D. C. Lev, R. E. Pollock, and K. V Larin, "Revealing retroperitoneal liposarcoma morphology using optical coherence tomography.," *J. Biomed. Opt.*, vol. 16, no. 2, p. 020502, Feb. 2011.

[8] S. S. Gao, R. Wang, P. D. Raphael, Y. Moayedi, A. K. Groves, J. Zuo, B. E. Applegate, and J. S. Oghalai, "Vibration of the organ of Corti within the cochlear apex in mice," *J. Neurophysiol.*, vol. 112, no. 5, pp. 1192–1204, Jun. 2014.

[9] A. F. Fercher, C. K. Hitzenberger, G. Kamp, and S. Y. El-Zaiat, "Measurement of intraocular distances by backscattering spectral interferometry," *Opt. Commun.*, vol. 117, no. 1–2, pp. 43–48, May 1995.

[10] R. Leitgeb, C. Hitzenberger, and A. Fercher, "Performance of fourier domain vs time domain optical coherence tomography," *Opt. Express*, vol. 11, no. 8, p. 889, Apr. 2003.

[11] M. Choma, M. Sarunic, C. Yang, and J. Izatt, "Sensitivity advantage of swept source and Fourier domain optical coherence tomography," *Opt. Express*, vol. 11, no. 18, p. 2183, Sep. 2003.

[12] A. F. Fercher, W. Drexler, C. K. Hitzenberger, and T. Lasser, "Optical

coherence tomography – development, principles, applications," *Z. Med. Phys.*, vol. 20, no. 4, pp. 251–276, 2010.

[13] D. Huang, E. Swanson, C. Lin, J. Schuman, W. Stinson, W. Chang, M. Hee, T. Flotte, K. Gregory, C. Puliafito, and al. et, "Optical coherence tomography," *Science (80-.).*, vol. 254, no. 5035, pp. 1178–1181, Nov. 1991.

[14] J. A. Izatt and M. A. Choma, "Theory of Optical Coherence Tomography," in *Optical Coherence Tomography*, 2nd ed., W. Drexler and J. G. Fujimoto, Eds. Springer International Publishing, 2008, pp. 47 – 72.

[15] W. Drexler, U. Morgner, F. X. Kärtner, C. Pitris, S. A. Boppart, X. D. Li, E. P. Ippen, and J. G. Fujimoto, "In vivo ultrahigh-resolution optical coherence tomography," *Opt. Lett.*, vol. 24, no. 17, p. 1221, Sep. 1999.

[16] H. Yabushita, "Characterization of Human Atherosclerosis by Optical Coherence Tomography," *Circulation*, vol. 106, no. 13, pp. 1640–1645, Sep. 2002.

[17] A. M. Rollins and J. A. Izatt, "Optimal interferometer designs for optical coherence tomography," *Opt. Lett.*, vol. 24, no. 21, p. 1484, Nov. 1999.

[18] Y. Zhao, Z. Chen, C. Saxer, S. Xiang, J. F. de Boer, and J. S. Nelson, "Phase-resolved optical coherence tomography and optical Doppler tomography for imaging blood flow in human skin with fast scanning speed

and high velocity sensitivity," *Opt. Lett.*, vol. 25, no. 2, p. 114, Jan. 2000.

[19] M. C. Pierce, B. Hyle Park, B. Cense, and J. F. de Boer, "Simultaneous intensity, birefringence, and flow measurements with high-speed fiber-based optical coherence tomography," *Opt. Lett.*, vol. 27, no. 17, p. 1534, Sep. 2002.

[20] Z. Chen, T. E. Milner, S. Srinivas, X. Wang, A. Malekafzali, M. J. C. van Gemert, and J. S. Nelson, "Noninvasive imaging of in vivo blood flow velocity using optical Doppler tomography," *Opt. Lett.*, vol. 22, no. 14, p. 1119, Jul. 1997.

[21] J. Kehlet Barton, J. A. Izatt, M. D. Kulkarni, S. Yazdanfar, and A. J. Welch, "Three-dimensional reconstruction of blood vessels from in vivo color Doppler optical coherence tomography images.," *Dermatology*, vol. 198, no. 4, pp. 355–61, Jan. 1999.

[22] J. A. Izatt, M. D. Kulkarni, S. Yazdanfar, J. K. Barton, and A. J. Welch, "In vivo bidirectional color Doppler flow imaging of picoliter blood volumes using optical coherence tomography.," *Opt. Lett.*, vol. 22, no. 18, pp. 1439–41, Sep. 1997.

[23] S. S. Gao, P. D. Raphael, R. Wang, J. Park, A. Xia, B. E. Applegate, and J. S. Oghalai, "In vivo vibrometry inside the apex of the mouse cochlea using spectral domain optical coherence tomography.," *Biomed. Opt.*

Express, vol. 4, no. 2, pp. 230–40, Feb. 2013.

[24] B. Vakoc, S. Yun, J. de Boer, G. Tearney, and B. Bouma, “Phase-resolved optical frequency domain imaging.,” *Opt. Express*, vol. 13, no. 14, pp. 5483–93, Jul. 2005.

[25] B. Braaf, K. A. Vermeer, V. A. D. P. Sicam, E. van Zeeburg, J. C. van Meurs, and J. F. de Boer, “Phase-stabilized optical frequency domain imaging at 1-µm for the measurement of blood flow in the human choroid.,” *Opt. Express*, vol. 19, no. 21, pp. 20886–903, Oct. 2011.

[26] M. A. Choma, A. K. Ellerbee, C. Yang, T. L. Creazzo, and J. A. Izatt, “Spectral-domain phase microscopy,” *Opt. Lett.*, vol. 30, no. 10, p. 1162, May 2005.

[27] A. L. Nuttall, D. F. Dolan, and G. Avinash, “Laser Doppler velocimetry of basilar membrane vibration,” *Hear. Res.*, vol. 51, no. 2, pp. 203–213, Feb. 1991.

[28] M. A. Ruggero and N. C. Rich, “Application of a commercially-manufactured Doppler-shift laser velocimeter to the measurement of basilar-membrane vibration,” *Hear. Res.*, vol. 51, no. 2, pp. 215–230, Feb. 1991.

[29] N. Stasche, H.-J. Foth, K. Hörmann, A. Baker, and C. Huthoff, “Middle Ear Transmission Disorders—Tympanic Membrane Vibration Analysis by

Laser-Doppler-Vibrometry," *Acta Otolaryngol.*, Jul. 2009.

[30] G. R. Ball, A. Huber, and R. L. Goode, "Scanning laser Doppler vibrometry of the middle ear ossicles.," *Ear. Nose. Throat J.*, vol. 76, no. 4, pp. 213–8, 220, 222, Apr. 1997.

[31] R. K. Wang and A. L. Nuttall, "Phase-sensitive optical coherence tomography imaging of the tissue motion within the organ of Corti at a subnanometer scale: a preliminary study.," *J. Biomed. Opt.*, vol. 15, no. 5, p. 056005, Jan. 2010.

[32] H. M. Subhash, A. Nguyen-Huynh, R. K. Wang, S. L. Jacques, N. Choudhury, and A. L. Nuttall, "Feasibility of spectral-domain phase-sensitive optical coherence tomography for middle ear vibrometry.," *J. Biomed. Opt.*, vol. 17, no. 6, p. 060505, Jun. 2012.

[33] S. S. Gao, A. Xia, T. Yuan, P. D. Raphael, R. L. Shelton, B. E. Applegate, and J. S. Oghalai, "Quantitative imaging of cochlear soft tissues in wild-type and hearing-impaired transgenic mice by spectral domain optical coherence tomography.," *Opt. Express*, vol. 19, no. 16, pp. 15415–28, Aug. 2011.

[34] G. V. Gelikonov, V. M. Gelikonov, and P. A. Shilyagin, "<title>Linear wave-number spectrometer for spectral domain optical coherence tomography</title>," in *Biomedical Optics (BiOS) 2008*, 2008, p. 68470N–

68470N–7.

[35] Z. Hu and A. M. Rollins, “Fourier domain optical coherence tomography with a linear-in-wavenumber spectrometer,” *Opt. Lett.*, vol. 32, no. 24, p. 3525, Dec. 2007.

[36] J. Xi, L. Huo, J. Li, and X. Li, “Generic real-time uniform K-space sampling method for high-speed swept-source optical coherence tomography.,” *Opt. Express*, vol. 18, no. 9, pp. 9511–7, Apr. 2010.

[37] M. P. Minneman, J. Ensher, M. Crawford, and D. Derickson, “All-semiconductor high-speed akinetic swept-source for OCT,” in *Communications and Photonics Conference and Exhibition, 2011. ACP. Asia*, 2011, p. 831116.

[38] M. Bonesi, M. P. Minneman, J. Ensher, B. Zabihian, H. Sattmann, P. Boschert, E. Hoover, R. A. Leitgeb, M. Crawford, and W. Drexler, “Akinetic all-semiconductor programmable swept-source at 1550 nm and 1310 nm with centimeters coherence length.,” *Opt. Express*, vol. 22, no. 3, pp. 2632–55, Feb. 2014.

[39] J. Park, E. F. Carbajal, X. Chen, J. S. Oghalai, and B. E. Applegate, “Phase-sensitive optical coherence tomography using an Vernier-tuned distributed Bragg reflector swept laser in the mouse middle ear.,” *Opt. Lett.*, vol. 39, no. 21, pp. 6233–6, Nov. 2014.

[40] S. Van der Jeught, J. J. J. Dirckx, J. R. M. Aerts, A. Bradu, A. G. H. Podoleanu, and J. A. N. Buytaert, “Full-field thickness distribution of human tympanic membrane obtained with optical coherence tomography.,” *J. Assoc. Res. Otolaryngol.*, vol. 14, no. 4, pp. 483–94, Aug. 2013.

[41] W. Dong, P. Varavva, and E. S. Olson, “Sound transmission along the ossicular chain in common wild-type laboratory mice.,” *Hear. Res.*, vol. 301, pp. 27–34, Jul. 2013.